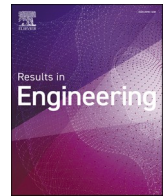---

To cite this version :

Chrysoula CHATZIGEORGIOU, Boris PIOTROWSKI, Fodil MERAGHNI, Yves CHEMISKY - Multiscale mechanical analysis for biomimetic implant design based on Triply Periodic Minimal Surfaces (TPMS) lattices: Application to partial replacement of femoral bone - Results in engineering - Vol. 25, p.103984 - 2025

Research paper

Multiscale mechanical analysis for biomimetic implant design based on Triply Periodic Minimal Surfaces (TPMS) lattices: Application to partial replacement of femoral bone

Chrysoula Chatzigeorgiou [a], Boris Piotrowski [a], Fodil Meraghni [a],* [ID], Yves Chemisky [b]

[a] *Arts et Métiers Institute of Technology, CNRS, Université de Lorraine, LEM3-UMR 7239 CNRS, 4 rue Augustin Fresnel, 57078 Metz, France*
[b] *Université de Bordeaux, I2M UMR CNRS 5295, Bordeaux, France*

ABSTRACT

Medical implants are a common treatment for orthopedic injuries. Their apparent stiffness can be reduced by using architected internal lattices to match the gradient stiffness of the bone, thereby avoiding postoperative biomechanical problems such as stress shielding. The use of TPMS-based lattice structures with smooth junctions offers the potential to tailor the apparent modulus of an implant while minimizing stress concentration throughout the microstructure. In this study, four TPMS-based unit cells are investigated, namely: Schoen's Gyroid-like (sheet and skeletal), Schwartz's Primitive, and Schoen's IWP topologies. The objective of the investigation is to numerically replace a small region of a femoral bone, hereafter referred to as the area of interest (AoI). Multiscale approach is proposed for the 3D model of the femur. The latter consists of the global model (femur bone) and the local model (TPMS unit cell). The unit cells are selected to satisfy the elastic and mechanical loading requirements and are compared according to the von Mises stress distribution after applying periodic boundary conditions. A statistical analysis is performed and a function factor is proposed to facilitate the comparison. The developed methodology allows the design of customized and patient-specific implants when a large medical database is used due to the varying size and shape of patients' bones.

1. Introduction

Medical implants are a common treatment for serious injuries and the need for orthopedic implants has been increased in the last few years. Orthopedic implants are specific medical devices that replace a whole or a part of the damaged bone while mimics their structure, density, mechanical properties, and function as much as possible. Patients' expectations are nowadays increasing as they expect to resume their daily activities after implant surgery, which impose higher requirements in terms of mechanical properties for the implant. For a successful implant surgery, both biological and mechanical requirements should be satisfied [1]. Therefore, it is crucial to solve any postoperative biomechanical problems that occur, such as stress shielding-related problems. Stress shielding is a biomechanical phenomenon causing adaptive changes in bone strength and stiffness around metallic implants, due to a mismatch in elastic properties between bone and implants [2]. This phenomenon is described by Wolff's law [3] and leads to a non-physiological development of the bone

density, which in turn leads to implant instability and pain [4–5]. The reduction of the stress shielding effect can be achieved in two ways. The first way is the choice of bulk material for the implant, with an apparent elastic modulus close to the Young's modulus of the natural bone [6–7]. The second solution consists of the design of a porous structure for the implant instead of a continuum bulk material, and thus the aforementioned material-dependent limitation could be overcome. The use of lattice structures offers the opportunity to control and tailor the apparent elastic modulus and overall mechanical properties of an implant. By designing an architectured implant, its apparent stiffness could be lower compared to the stiffness of a compact implant and thus closer to the levels of the human bone [8]. Architectured structures offer the possibility to overcome material-dependent limitation by adapting their geometry, i.e. macro-porosity, to the elastic requirements of each application [9]. Therefore, lattices can replace certain parts or a whole biomedical device and allow the construction of architectured implants. Lattice structures exhibit a strictly constructed and defined topology. Their topology is periodic and it consists of several repeating cubic unit

* Corresponding author.
E-mail address: fodil.meraghni@ensam.eu (F. Meraghni).

cells at a row throughout all three directions. A unit cell is the smallest part of a lattice that represents all the morphological details, as well as the overall behaviour. It can be repeated periodically to create a complete lattice. Control over all the morphological details of the unit cells means control over the overall elastic response of an implant [10–11]. The lattices based on the Triply Periodic Minimal Surfaces (TPMS) are biomimetic because they can be found in nature. Unlike strut-based lattices, which have sharp edges, TMPS structures are generated topologies that have smooth connections at the vertices [12–16]. These structures have been mechanically characterised to relate the effective mechanical properties to the geometric parameters, for uniform morphologies [17,18] or multi-morphological structures [19–20].

In order to successfully mimic the material properties of the real human bone and to construct custom-made and patient-specific implants, medical data are required. They contain patient-specific information because the size and shape of the bones and the joints vary from person to person depending on age, gender, height, etc. [21]. In addition, the elastic modulus of a bone is not a constant value. It varies in the global range of $0.02-30\ GPa$ according to the bone structure, i.e. cancellous or cortical, and according to the direction, i.e. longitudinal or transverse [22–23]. Patient-specific implants would allow to specifically tailor the local mechanical properties, especially when severe bone structure differences are observed. The custom-made and patient-specific implants offer a promising option to treat hip diseases in a more tailored way, minimize recovery time and overall procedural costs, and improve the patients' outcome [24–26]. Recent studies have demonstrated the ability to mimic the behaviour of cortical (or cortical and trabecular) bone using TPMS structures [27–29]. Yang et al. [30] has even suggested several adaptations to titanium unit cells to mimic the biomechanical response of bones, using morphologic modifications of the original TPMS by applying shear of torsion geometrical transformation. On a different aspect, other functionalities such as allowing bone ingrowth and/or nutriments transport is another advantage of TPMS structures. In [31], it has been shown that the open-porous characteristics TPMS microstructures is a key factor to enhance bone tissue ingrowth from an in-vivo study. For instance, the Diamond based scaffold has shown a higher bone colonization than other TPMS structures tested.

Regarding the fabrication of custom implants, additive manufacturing technology makes it easy to produce complex, free-form geometries and shapes [32–33]. Rezapourian et al. has investigated the mechanical properties of SLM-fabricated Ti6Al4V Gyroid TPMS lattice structures for bone tissue engineering, highlighting the potential of Gyroid lattices for bone replacements due to their tailored mechanical and biological responses [34]. Collecting and exchanging medical data is done using the developed international standard Digital Imaging and COmmunications in Medicine (DICOM). The images with the DICOM format represent the scanned area of a human body at three planes, i.e. the sagittal, coronal, and axial planes, and all the morphological features of the hard and soft tissues are portrayed [24]. They are grayscale images in Hounsfield Units (HU), which allow quantitative measurement of radiodensity. Dense tissues with high HU, such as bone, are shown in white, while tissues with lower HU, such as fat and muscle, are shown in various shades of grey. Air is represented by black color [35–37]. Many researchers have investigated the correlation between HU and the elastic modulus of various human tissues as reported in [38–41].

To the best of our knowledge, no previous study has performed a multiscale simulation and stress analysis of TPMS-based biomimetic implants and a femoral bone generated by real DICOM images and subjected to actual loading configuration. The present study is a contribution to the field of BTE (Bone Tissue Engineering), it aims to provide bioengineers with the multiscale simulation methodology to reduce the need for resource-intensive physical experiments. Indeed, as reported in the relevant recent paper by Bazyar and Sheidaee [42], modeling and simulation in BTE have an exceptional utility in evaluating and validating experiments conducted in vitro and in vivo. To this

end, this work proposes a multiscale simulation and stress analysis aimed at comparing four different TPMS-based unit cells for a partial femoral bone replacement by selecting of the most appropriate topology. The four structures were adopted on the basis of the results of a previous study [17]. The developed methodology can be generalized to mimic other physiological configurations. In the present paper, the developed approach focuses on developing comprehensive methodology to numerically design and study a real femoral bone in an actual loading configuration. Four TPMS-based lattices namely the Schoen's Gyroid-like (sheet and skeletal), Schwartz's Primitive, and Schoen's IWP topologies have been analyzed and compared towards a partial femoral bone replacement. The finite element analysis is performed at two scales; the global scale considers the physiological load on a femoral bone while the local scale focuses on the AoI subjected to the kinematic field extracted from the global analysis. The AoI corresponds to the region that requires the bone replacement by a TPMS-based implant. It is worth mentioning that the loading configuration represents a low speed walking and does not consider the durability aspect (fatigue limit). Besides this introductory section, the paper is organized as follows. The second section describes the procedure for generating of the global and local numerical models and the stress distribution on the TPMS-based unit cells. The third section presents the generated results and the comparison of the investigated TPMS-based topologies in terms of local stress. The discussion of the results is detailed in the fourth section. The concluding remarks of the study are presented in the last section of this paper. In the latter, some pertinent perspectives are drawn as the next steps of the present work.

2. Global to local approach and related numerical methods

This section describes the steps of the implemented numerical methodology in a real case study. The methodology is divided into two parts, the generation of the global and local models for FEA, respectively. The global-scale analysis is a finite element analysis carried out at the scale of a bone, on physiological boundary conditions representative of a real load (described in the next sub-sections). The local-scale analysis is also a finite-element analysis, on the scale of a bone VER. The boundary conditions applied in this local case, detailed in the corresponding section, are derived from the results of the global-scale analysis. The approach of the multiscale simulation is schematically shown in Fig. 1.

The creation of the global model is based on DICOM images for the geometric model and the assignment of the material properties. The applied boundary conditions correspond to the physiological loading of a femoral bone and they have been obtained from experimental tests on real patients reported in a public database [43]. The generation of the TPMS microstructure is based on local elastic properties of the global model, i.e. the elastic properties of the bone to be replaced, determined from the density identified in the DICOM images. The local applied boundary conditions arise from the Finite Element Analysis (FEA) of the femoral bone subjected to the physiological prescribed loading. Details about those steps of the methodology are given in the following sections.

2.1. Global 3D model

2.1.1. Geometric design and assignment of material properties

The first step is to generate of a macroscopic 3D model consisting of a femur bone. As part of a scientific collaboration with the Institut de Biomécanique Humaine Georges Charpak (IBHGC) laboratory, medical images in a DICOM format from an anonymous female patient were used in this study. The stack of DICOM images is imported into the Materialise Mimics software. The segmentation of the images starts with the creation of a mask representing a femur bone based on the HU of the real cortical bone, i.e. $HU \geq 700$ [40]. The internal cavity corresponding to the trabecular bone has a lower HU. A manual segmentation is operated in each image and finally merged with the initial mask to describe the
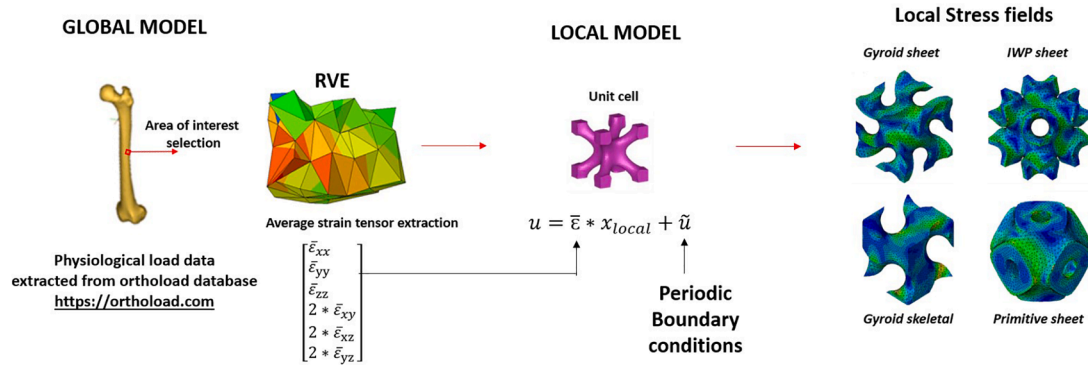
Fig. 1. Schematic form of the partial bone replacement methodology by replacing an RVE with a volume with a single TPMS-based unit cell. $\bar{\varepsilon}$ refers to average strain tensor in RVE, and $\tilde{u}$ stands for the periodic displacement applied at the boundary of the TPMS-based unit cell (periodic boundary conditions).

entire femur bone, including both cancellous and cortical structures. The 3D model is generated and is exported as a surface mesh. Further correction and repair are generally necessary at this point. In this study, the software Materialise's 3-matic has been utilized to optimize the quality of the surface mesh, based on linear triangles. The FE volume mesh is then generated with C3D4 tetrahedral elements based on the surface mesh. An analysis of the mesh element size on numerical accuracy has been performed. The selection of C3D4-type elements for the global model is dictated by the numerical tools used to export the DICOM geometry, which has been meshed prior to the export process.

The elastic material properties are assigned by combining the information from the DICOM images and the volume mesh. In particular, Chougule et al. [40] presents a table with the typical range of the HU for different human tissues for both adults and children. The HU values corresponding to cortical and trabecular bone for adults have been selected accordingly considering the following ranges: The first HU range corresponds to the cortical bone and it is defined as $HU_{cortical} \geq 700\ HU$. The second area corresponds to the trabecular bone and it is defined as $150\ HU \leq HU_{trabecular} \leq 700\ HU$. The third HU range corresponds to the soft tissues, such as muscle and fat, and it includes the

lowest positive HU values and also the negative ones as well.

For the general case of the cortical bone, a linear relationship between the elastic modulus and the density described by the HU gives accurate results according to [39]. Three different elastic modulus ranges classically describe the cortical bone in the longitudinal and two transverse directions. However, in this case study, the elastic properties of the bone are assumed to be linear and only one elastic modulus range is applied to the cortical bone, which is set between $10-18\ GPa$ to account for both the high and the low elastic modulus of the femoral cortical bone in all directions, following [44–45]. Therefore, a different elastic modulus value is applied to each element according to the intensity of the gray level (HU) and to a linear law where $E_{min} = 10,000\ MPa$ and $E_{max} = 18,000\ MPa$. The repartition of elastic modulus is discretized considering ten subdivisions of 800 MPa. In this way, 10 different materials are created in the finite element model and assigned (average Young's modulus of 10,400 MPa for volumes between 10,000 and 10,800 MPa, Young's modulus of 11,200 for volumes between 10,800 and 11,600 MPa…). The Young modulus selected for each discrete value and the corresponding area of the femoral bone is shown in Fig. 2a.

Color	E (MPa)
	10399.9
	11199.8
	11999.6
	12799.5
	13599.3
	14399.1
	15199
	15998.8
	16798.7
	17598.5

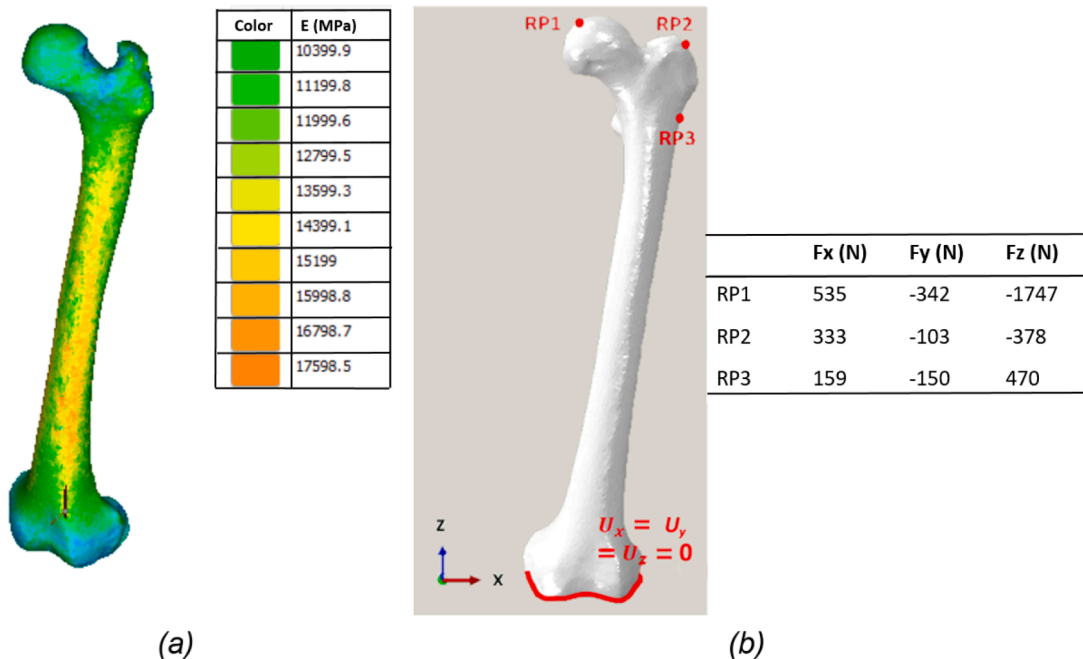|	Fx (N)	Fy (N)	Fz (N)
RP1	535	-342	-1747
RP2	333	-103	-378
RP3	159	-150	470

(a)   *(b)*

Fig. 2. (a)Ten subdivisions of the material type corresponding to the elastic modulus of the cortical bone and femoral bone after assigning material properties in Materialise Mimics software - (b)The complete numerical model of the femoral bone in Abaqus and the values of the muscular forces applied to the reference points RP2 and RP3.

Regarding the specific case of the femoral trabecular bone, a set of equations has been used to relate the HU, which describes the density, and the applied elastic modulus according to [39], where several equations are proposed for a number of different bones. The following relationship has been consequently applied in this study:

$$\rho = f_{gray} * HU_{trabecular} + \rho_0 \tag{1}$$

$$E = K * \rho^n \tag{2}$$

Where ρ is the density described by the HU and E is the elastic modulus applied to each element. The apparent density (ρ) is computed from the CT gray values converted into Hounsfield units (HU), using a linear calibration derived from two reference points (water and air). The factor f_{gray} represents an empirical relationship between the gray level and the density of the bone, since the bone density is directly related to gray level in DICOM images. Also, ρ_0 describes a limit of density that is not captured by DICOM images, where the gray level is close to zero. The calibration of density of cancellous bone was determined by [39] considering a measured density of cancellous bones as wet weight divided by volume of the overall physical dimensions of the specimens. A second empirical relationship is often given between the density and the Young's modulus of bone, using a power-law of proportionaly factor K and exponent n. The units are deliberately not specified here since all these factors describe empirical relationship with no precise physical insight. In [39], it has been shown that such a power-law represent with a good accuracy the elastic response of samples, estimated using pulse transmission ultrasonic technique. The following values were adapted from [39] to describe the elastic response of femur cancellous bone: $K = 0.25$ and $n = 1.3$. Note that for the elements with HU < 150, if any, the stiffness related to such tissue is neglected.

2.1.2. Loading case, the walking

A femoral bone is typically subjected to a complex load that varies depending on the activity performed by the individual, such as walking, stair climbing stairs, jumping, and jogging. A combination of skeletal and muscular forces results in the final complex load as explained in [46]. In this case, the walking loading case was selected. In order to define the boundary conditions to use for the FE analysis of a complete femur bone, it is necessary to calculate the resultant hip contact force F_{RES} and its components F_x, F_y, and F_z. The database https://orthoload.com [43] collects various data obtained from in vivo tests on patients with hip implants performing various common everyday activities. The methodology for calculating F_{RES} described in [46–47] is applied to ten patients, and the final F_{RES} signals are averaged and adjusted to a body mass of 75 kg, which is the average weight of people in Europe. The aforementioned data and methodology have been combined in [48] where the maximum F_{RES} is calculated. This F_{RES} is also utilized in this study as well. The selected forces for the application to a FE model are as follows: $F_{RES} = 1859\ N$, $F_x = 535\ N$, $F_y = -342\ N$, $F_z = -1747\ N$. In addition, all the displacements and rotations in all three directions at the lowest part of the femur, i.e. the knee joint have been blocked for the mechanical equilibrium.

The next step is to define the muscular forces to which the femoral bone is subjected. The data taken from the database https://orthoload.com [43], the CT scan data from Visible Human [49], and the methodology described in [46] are combined in [48] where the simplified muscular forces are calculated. Those muscular forces are selected and used in this study. The complete 3D numerical model and the values of the forces are shown in Fig. 2b. RP1 is a reference point where the F_{RES} is applied and RP2 and RP3 are the reference points where the muscular forces are applied. These points are considered to be the center of the area of the insertion surface (muscle-bone connection), the geometric position is also specified by orthoload database. All the degrees of freedom of these three reference points and the corresponding nodes around them have been constrained to be connected. This is carried out to avoid any singularities and non-realistic final results caused by the

application of the boundary conditions. The lower part of the femur is completely clamped, where the following displacement conditions is applied: $U_1 = U_2 = U_3 = UR_1 = UR_2 = UR_3 = 0$ are applied. The following step is the creation of an element set which is actually the Area of Interest (AoI) in the bone. This is detailed in the following section.

The entire model is defined in the FEA software Abaqus to solve the boundary value problem detailed in this section.

2.1.3. Definition of the area of interest (AoI)

The AoI was chosen to correspond to a portion of the cortical bone of a femur that is to be replaced by a RVE (Representative Volume Element). The latter should satisfy the elastic requirements of the cortical bone to obtain a successful replacement without the occurrence of the stress shielding problem. When the area to be replaced exceeds a RVE, or when there are multiple areas to replace, the same methodology is applied repeatedly for each RVE. The set of elements is placed close to the perimeter of the femoral stem so that the AoI corresponds to a part of the cortical bone, with a volume of about 275 mm³. The areas where the stresses are computed must be sufficiently far away from the region of application of nodal forces as required by the Saint-Venant's principle. The elements of the AoI have different elastic moduli according to the HU and the material assignment as described above. The elastic moduli of all the elements of the AoI vary in the range of the elastic modulus of the cortical bone. An average value, E_{AoI}, is then computed and it is set as the target for the RVE design. The elements have been manually selected so that the shape of the element is as close as possible to a cubic shape. This method can be applied in a general way to any area of the bone. The area of interest is highlighted in Fig. 3.

Once the FEA of the femoral bone is complete, the average strain tensor of the AoI is computed following the Eq. (3):

$$\left[\overline{\varepsilon}_{ij}\right] = \frac{1}{V_{total}} \sum_{k=1}^{N} \left(\varepsilon_{ij}\right)_k * v_k \tag{3}$$

Where $\overline{\varepsilon}_{ij}$ corresponds to the components of the average strain tensor, N is the total number of elements, $\left(\varepsilon_{ij}\right)_k$ is the strain of each element, v_k is the volume of each element, and V_{total} is the total volume of the AoI. The complete average strain tensor is then applied to a single unit cell by using Periodic Boundary Conditions (PBC) in a mixed loading case to determine the average loading over the tissue to be replaced considering the realistic walking loading case. All the details about the creation of the local models and the FEA are given in the following section.

2.2. Local 3D model

The objective is next to design unit cells with the same elastic modulus as the corresponding of the AoI. This is performed to successfully replace the AoI by the unit cells taking into account the stress shielding minimization.

The design methodology and the numerical estimation of the design parameters and the elastic properties of the unit cells are detailed in our previous study [17] and the normalized results are presented in graphs. level-set equations based on trigonometric functions in the form of $f(x, y, z) = t$, where t is a constant value, are used for an accurate approximation of the TPMS [50]. The value of the t parameter controls the offset of the minimal surfaces and thus the volume fraction of the generated unit cells and lattices [17]. The normalized value of the E_{AoI} allow the determination of the design parameter t for several TPMS topologies.

Four different topologies, namely Gyroid sheet, IWP sheet, Gyroid skeletal, and Primitive sheet, were selected and the relevant cubic unit cells were designed according to the methodology described in [17]. All four unit cells satisfy the elastic requirements of the AoI, i.e. they have the same elastic modulus as the E_{AoI}. The volume fraction of the unit cells varies according to the chosen topology. The size of the unit cells is similar to the average size of the AoI, even though the size does not have
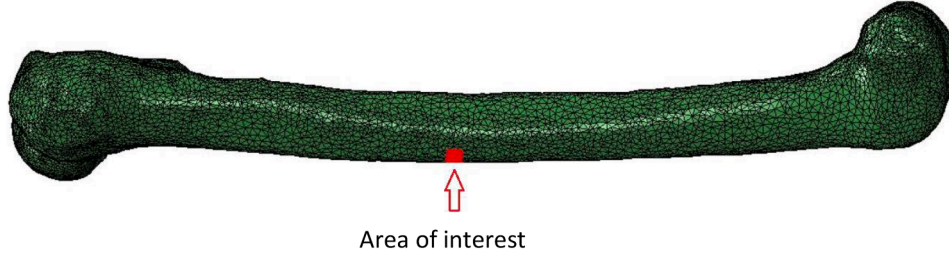
Fig. 3. Highlighted element set that corresponds to the area of interest in the femoral bone.

an impact since the application of the periodic boundary conditions described below render the simulation of the unit cell insensitive to the dimensions (only the geometric shape of the microstructure matters). The parameters (t) adopted to design the structure of Gyroid sheet, IWP sheet, Gyroid skeletal, and Primitive sheet [17] are 0.48, 1.06, 0.34 and 0.63 respectively, whereas the respective volume fraction are 0.382, 0.344, 0.443 and 0.414.

For the local model, the mesh was generated using Abaqus software. C3D10 quadratic interpolation elements were adopted. For the example of the gyroid structure, 55,525 elements were generated (for a total of 83,412 nodes). A mesh convergence analysis was carried out, and the tetrahedral shape elements adopted exhibit an average size of 0.24 mm, for a structure with a volume of $6.5 \times 6.5 \times 6.5$ mm^3. The applied material properties are the following: $E = 85,000$ MPa and $v = 0.3$. these properties have been experimentally determined on Ti-6Al-4 V alloy samples obtained by additive manufacturing using SLM process. The calculated average strain tensor (Eq. (3)) is imposed as input to all unit cells considering periodic boundary conditions in a single, mixed loading case by using the constraint driver approach [51]. In particular, a FE-compatible periodic homogenization method [52] is implemented on the unit cells, which are considered as the microscopic scale of the problem.

Assuming that the RVE can be represented as a repeating element, it can be idealized as a periodic unit cell in which the displacement field u (x) takes the following additive formulation:

$$u(x) = \overline{\varepsilon} \cdot x + u'(x) + u_0 \quad \forall x \in V \tag{4}$$

where the first term ($\overline{\varepsilon} \cdot x$) depicts the affine partition of the displacement field, while the second term $u'(x)$, represents a periodic fluctuation that maintains identical values at each pair of opposite points within the RVE boundary (∂V).

$$u'(x_+) = u'(x_-) \quad \forall x_+, \ x_- \in \partial V \tag{5}$$

It is worth noticing that, due to its periodicity, the part of the strain associated with $u'(x)$, vanishes once averaged, ensuring a full consistency of the homogenization approach. The third term (u_0) stands for an eventual rigid body motion.

In this work, the homogenization problem is computationally solved through the finite element method, using periodically meshed unit cells. This numerical methodology using constraints drivers and periodic boundary conditions has already been applied for TPMS by the authors [17], where the relative equations are detailed.

The lattices and thus, the architectured implants are considered as the macroscopic scale of the problem.

The average von Mises stress σ_{avg} per topology is calculated and the full stress ranges are also recorded. The σ_{avg} is compared with the σ_{yield} of the bulk material of the unit cells and the average stress of the AoI is carried out. In addition, the local stress distribution of the unit cells should be considered in the design process of the architectured implants and medical devices to select the most appropriate topology in this quasi-static case. Therefore, the stress distribution over the population of the finite elements is calculated for all the studied topologies. Then, a statistical analysis is performed for a global comparison of the stress state between the investigated unit cells and the AoI. In the following section all the results are presented, compared and a complete analysis is performed.

3. Results and comparison

This section presents all the numerical results generated for the global and local models in terms of stress state and the statistical analysis. First, the qualitative results regarding the von Mises stress over the global model are presented and then, the quantitative results regarding the AoI as well. Then, the statistical results are presented for the investigated unit cell topologies considering an iso-elastic effective modulus case and the topologies are compared in a multi-parametric way.

3.1. Global model

To demonstrate the potential of application in personalized healthcare, the geometry of the global model is based on real morphological data from DICOM images for a anonymous specific patient. As presented in Section 2, the elastic modulus distribution of the global model corresponds to the real density described by the HU, and the applied boundary conditions correspond to a real, physiological loading case, i. e. walking. Note that the proposed methodology can be easily applied to any other physiological loading case and patients as well.

Furthermore, the application of the average strain tensor obtained from the global model combined with the PBC provides an accurate approximation of the physiological load on a portion of the femoral bone. An AoI can be defined anywhere in the model that represents an area to be replaced by an implant. Here, an AoI is defined on a portion of the femoral bone. In this case study, the average elastic modulus of the AoI is calculated and the result is $E_{AoI} = 13,798$ MPa. This value of the young's modulus is within the commonly accepted range for cortical bone, between $10 - 18$ GPa [22,44–45]. It is worth noticing that it remains as an input parameter that could be modified for medical consideration (e.g. surgeon recommendations).

The E_{AoI} is then normalized with respect to the alloy bulk modulus and the normalized value is $E'_{AoI} = 0.1623$. Normalization enables solutions to be obtained that are not dependent on the materials chosen for the implant. The solution can be adapted for each material by multiplying the Young modulus of the adopted alloy.

In terms of numerical results, this study focuses on the von Mises stress of the investigated models. Fig. 4 shows the von Mises stress contours of the whole femur and the AoI, along with the contour legends.

This is considered as a common configuration that corresponds to the applied forces on a femur when a person walks. The femoral stem is subjected to higher stresses than the upper and lower parts of the bone, as shown in Fig. 4. The von Mises stress for the entire femur in the range of $0 - 90$ MPa is shown in the contour legend. The AoI is here a representative part of the cortical bone in terms of both elasticity and stress state. The von Mises stress for the AoI varies in the range of $0 - 30$ MPa and the average stress value calculated at the centroid is $\sigma_{AoI\_AVG} =$
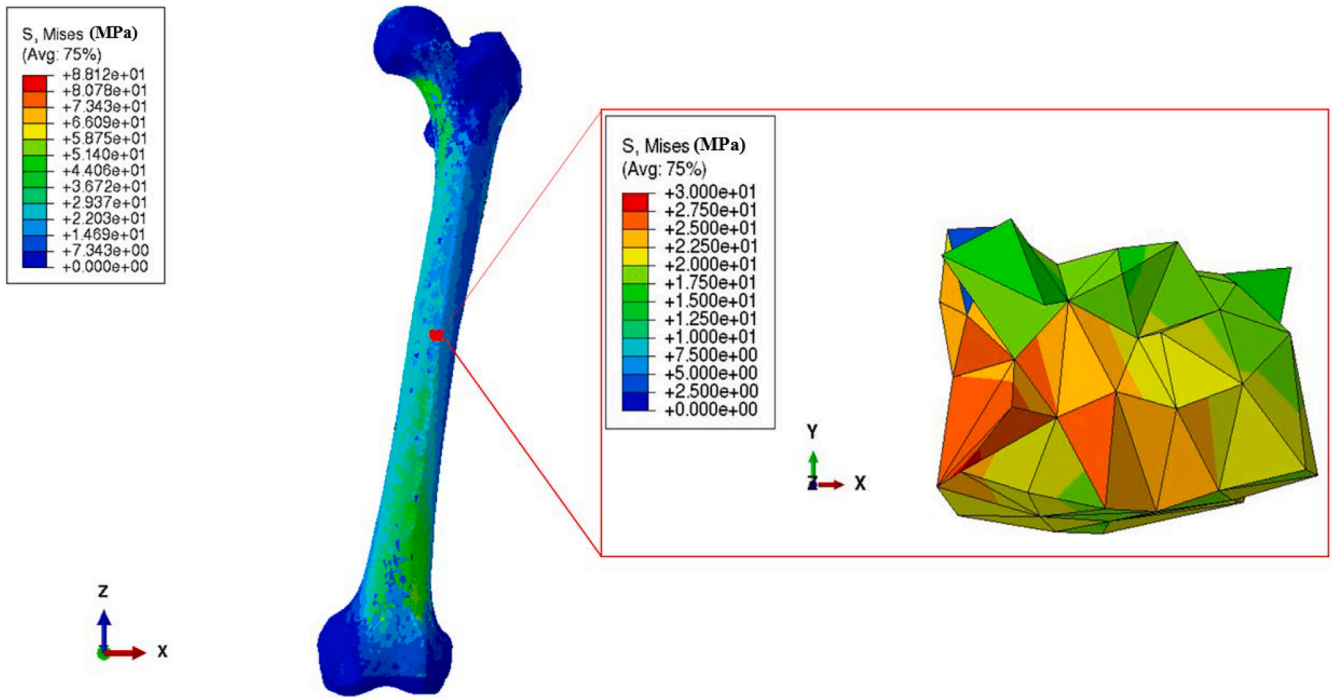
Fig. 4. Von Mises stress contour of the whole femur and the AoI and the relevant contour legends.

21.662 *MPa.*In addition, after the FEA, the average strain tensor of the AoI is also calculated, which is:

$$
\begin{bmatrix}
\bar{\varepsilon}_{xx} \\
\bar{\varepsilon}_{yy} \\
\bar{\varepsilon}_{zz} \\
2*\bar{\varepsilon}_{xy} \\
2*\bar{\varepsilon}_{xz} \\
2*\bar{\varepsilon}_{yz}
\end{bmatrix}
=
\begin{bmatrix}
-5.47*10^{-4} \\
-3.27*10^{-4} \\
-12.98*10^{-4} \\
-1.05*10^{-4} \\
-11.53*10^{-4} \\
-1.45*10^{-4}
\end{bmatrix}
$$

.

The global model was used as a reference for the creation of the local models in terms of stiffness and boundary condition requirements. The results for the investigated unit cells follow in the next section.

3.2. Local stress distribution: iso-elastic case

The effective elastic moduli of the selected unit cells are in accordance with the elastic modulus of the AoI. However, the volume fraction of the unit cells is topology-dependent. Fig. 5 shows all the investigated unit cell topologies and their respective volume fractions.

FEA has been performed for all four topologies by applying the average strain tensor to the unit cells in a mixed loading case considering periodic boundary conditions. This analysis is carried out to estimate the von Mises stress range and average stress values. Fig. 6 displays the von Mises stress contours for Gyroid sheet (a), IWP sheet (b), Gyroid skeletal (c), and Primitive sheet unit cells (d).

The average stress values for all the unit cells and the AoI are presented in Table 1. Note that differences are observed in the average von Mises equivalent stress, even if the effective Young's modulus and boundary conditions are the same. The simulations have been performed on an iso-Young modulus on the three directions of periodicity. First, a higher density will distribute the average stress of the whole cubic unit cell among a higher volume of material. The gyroid skeletal that has the highest density therefore presents the lower average stress. Additionally, each microstructure presents a different cubic anisotropy, such that the shear modulus and Poisson ration are not the same [17]. This can also affect the results since a non-negligible shear component of the effective
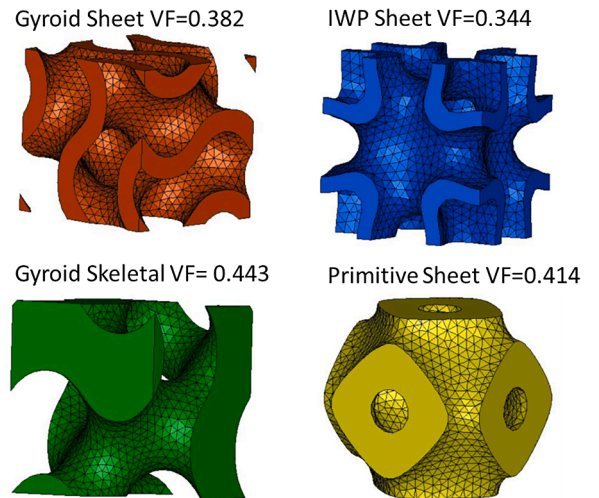

Fig. 5. Four investigated topologies with the same elastic modulus as the AoI and the corresponding volume fractions. a) Gyroid sheet, b) IWP sheet, c) Gyroid skeletal, and d) Primitive sheet unit cells.

strain is prescribed.

Furthermore, the local stress distribution over the range $0-350$ MPa is computed for all the unit cells considering periodic boundary conditions in a mixed loading case. Statistical analysis is then performed considering the normalized stress distribution over the range $0-1$ for all studied topologies in order to simplify the calculations. The weighted arithmetic mean and standard deviation, SD, are calculated to complete the quantitative comparison of the topologies. Since local stress is related to fatigue, the distributions of local stress are compared between the four considered TPMS. Fig. 7 shows those stress distributions over the population of finite elements for the unit cells with the same apparent Young modulus. The statistically computed values of weighted arithmetic mean and weighted standard deviation (SD) are presented in Table 2.
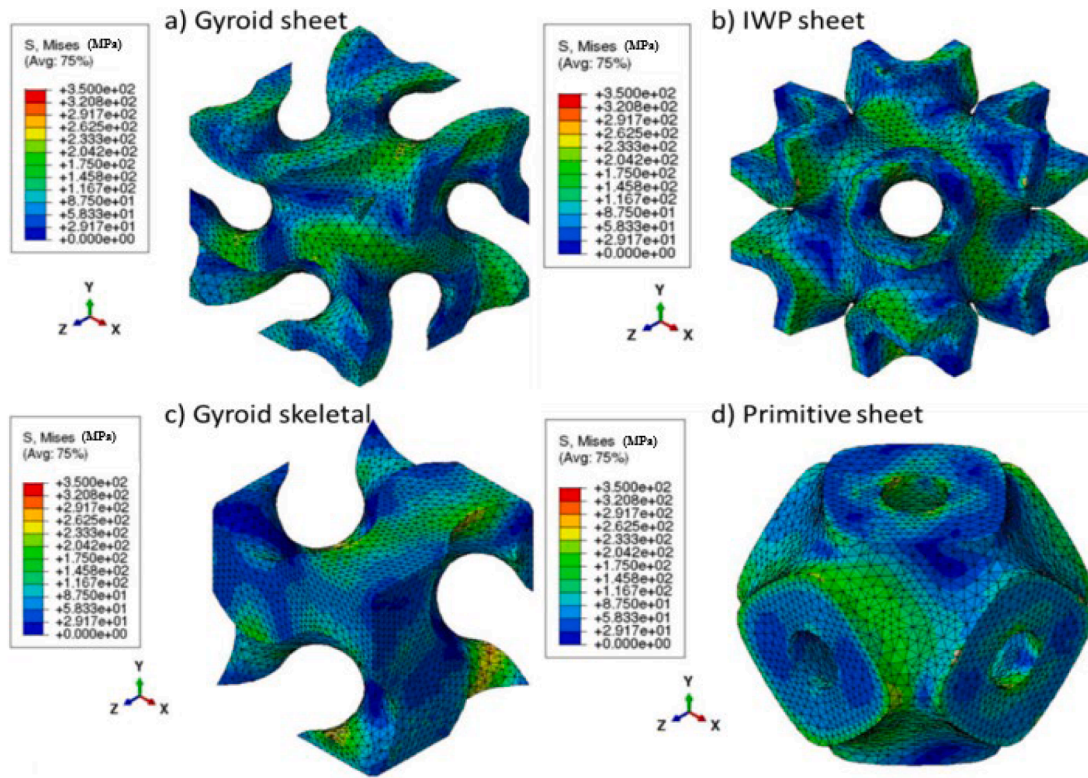
Fig. 6. Von Mises stress contours (MPa) for a) Gyroid sheet, b) IWP sheet, c) Gyroid skeletal, and d) Primitive sheet unit cells. It is worth noting that the TPMS-based topology prevents any stress concentration, even if the stress ranges from 0 to 350 MPa, as indicated in the contour legend.

Table 1
The average stress values at the centroid of the elements for all the studied unit cells and the AoI.

Topology	Average Stress [MPa]
Gyroid sheet	79.12
Gyroid skeletal	74.28
IWP sheet	81.62
Primitive sheet	81.79

Table 2
The table summarizes the weighted arithmetic mean, and weighted standard deviation (SD) of the investigated normalized local stress distributions and the volume fraction (V_F) of the analyzed topologies.

	Weighted arithmetic mean	Weighted SD	V_F
Gyroid skeletal	0.235	0.115	0.443
Gyroid sheet	0.255	0.121	0.382
IWP sheet	0.262	0.114	0.344
Primitive sheet	0.263	0.093	0.414

Note that the maximal stress amplitude is an interesting feature to be investigated. Indeed, it can lead to damage initiation and early failure of the implant. Considering that aspect, the Gyroid skeletal exhibit few areas with local stress that range between 200 and 250 MPa, that is not observed in other studied samples. The gyroid sheet exhibit also areas between 170 MPa to 220 MPa. On the other hand, local stress significantly drops for the IWP and Primitive sheet, with a maximum stress magnitude of 200 MPa. While the difference is not very significant, those two microstructures exhibit the lowest standard deviation, which indicates that most of the local stress values are close to the average stress magnitude. They therefore appear to be good candidates if failure prevention is a first-order design criterion.

To provide further insight about fatigue design analysis, we consider a damage initiation stress value set to 150 MPa. The sum of the stress occurrences above 150 MPa is calculated. This sum defines the R-factor, which differs according to the investigated structures. The value of 150 MPa is adopted so that the stresses above this value are significantly higher than the average stress value. To compare the structures, it is also intended to have an apparent effective density close to bone, i.e. a volume fraction of 0.4 considering the bulk density of titanium. Fig. 8 exhibits the R-factor of the structures as a function of the volume fraction gap between the TMPS structure and the physiological case.

As a benefit of this analysis, an orthopaedic surgeon interested in
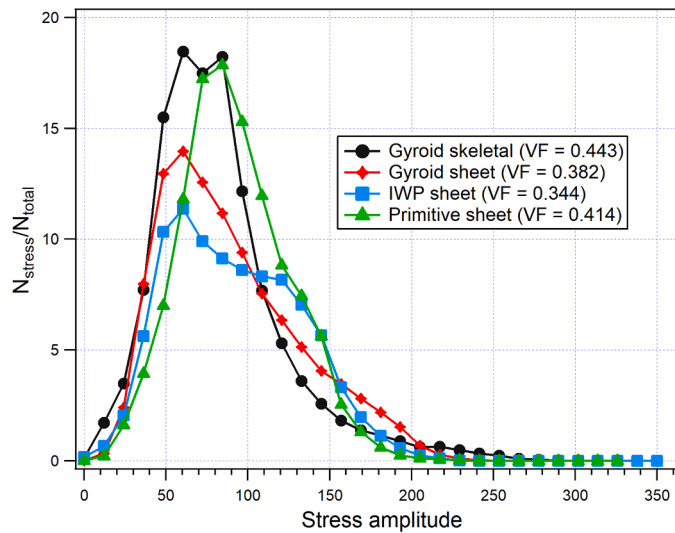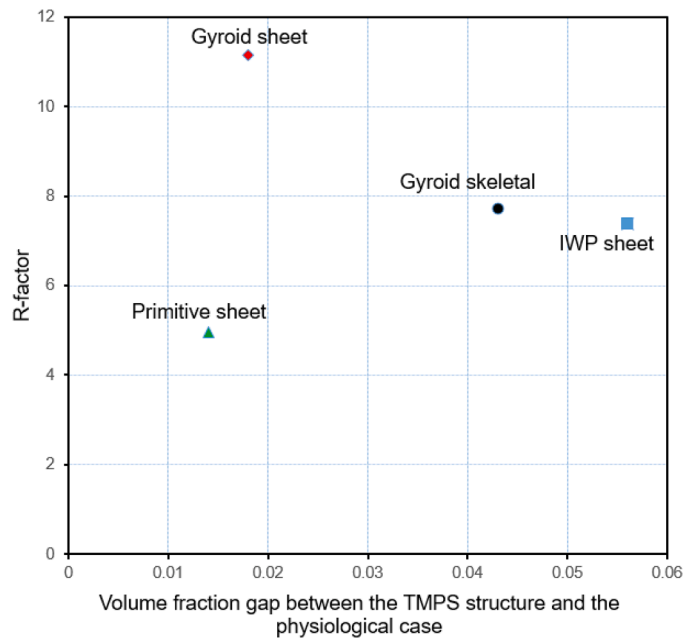

Fig. 7. Local stress distributions of Gyroid skeletal, Gyroid sheet, IWP sheet, and Primitive sheet unit cells at the same apparent Elastic modulus, $E_{AoI} = 13,798\ MPa$.

Fig. 8. R-factor of the structures as a function of the volume fraction gap between the TMPS structure and the physiological case.

replacing a part of a bone with TPMS-based lattices could use the statistical findings and graph presented above. Moreover, the Table 3 summarizes the R-factor of investigated structures to select the most suitable topology in a particular case with the advice of an engineer.

4. Discussion and analysis

It is worth noting that the periodic homogenization should normally be applied when the assumption of the scale separation, $\overline{x} \gg x$, is verified. In the particular case studied in this paper, this assumption is not strictly fulfilled in all implant directions. In fact, even though the size of the unit cells is much smaller than the size of the whole bone, the number of unit cell repetitions of a lattice that could be used as an implant cannot be large enough in all three directions of the bone. The Young's modulus in the longitudinal direction is approximately the same, although it varies with position. Therefore, the number of unit cell repetitions in this single direction could be appropriate in terms of periodic homogenization. On the contrary, the Young's modulus in the radial directions has a large variation due to the changes in bone structure from cortical to trabecular. Therefore, the number of periodic unit cells with the same apparent stiffness in the radial directions is very limited, and the scale separation assumption is partially not fulfilled. Therefore, the PBC were chosen as the boundary conditions that lead to consistent results in terms of the apparent modulus of the unit cells even though the scale separation assumption is partially relaxed. Furthermore, the application of the average strain tensor combined with the PBC acquired by the global model offers an accurate approximation of the physiological load on a part of the femoral bone

In Fig. 7, the stress distributions on the unit cells after the application of a physiological average strain in combination with the PBC are qualitatively compared. The stress distribution is topology-dependent

Table 3
The results of the R-factor, for the studied topologies.

Topology	V$_F$ gap between structure and physiological case	R-factor
Gyroid sheet	0.018	11.14
Gyroid skeletal	0.043	7.73
IWP sheet	0.056	7.38
Primitive sheet	0.014	4.95

and the stress values vary in the range of $0 - 350$ MPa. The maximum value which is the upper limit of the stress range, i.e. $\sigma_{max} = 350$ MPa, is lower than the yield stress of the Ti-6Al-4 V alloy, namely: $\sigma_{yield\_Bulk} = 830$ MPa [53]. The latter is the constitutive bulk material whose elastic properties have been utilized for the numerical analysis of the implant unit cells. Therefore, all topologies are able to mimic the local apparent modulus of the AoI without being subjected to local stresses exceeding the yield stress (σ_{yield_Bulk}), thus keeping the implant in the linear regime of the constituent material.

As presented in Table 1, The σ_{Bone} is the average stress that corresponds to the AoI and is shown to be the lowest among all the computed stress values. Although the von Mises stress is distributed in the range of $0 - 350$ MPa, the σ_{AVG} is presented to be much lower than the upper limit for all the topologies. This means that the majority of the elements are subjected to low stress as illustrated in Fig. 7. The minimum stress value which is closer to the σ_{Bone} is presented by the Gyroid skeletal topology whereas the maximum is presented by the Primitive sheet. Therefore, Gyroid skeletal would be selected as the best-fit geometry when the lowest average stress is the most important strength criterion.

As shown in Fig. 7, the topology of the unit cells induces different local stress distributions which could play an important role in this quasi-static loading case of the implants. All stress distributions present a weighted arithmetic mean between 0.235 and 0.263. The standard deviation (SD) shows how broad or narrow is a stress distribution. Therefore, the SD plays the role as stress distribution indicator of the apparent σ_{max} of the unit cells. As all the unit cells have been numerically studied with the same bulk material properties, some elements of the unit cells with a high standard deviation are subjected to higher stresses compared to those of the unit cells with a low SD. This means that among the studied structures, the apparent σ_{max} of the Gyroid sheet is closer to the apparent σ_{yield} and thus, closer to the plastic deformation. On the contrary, the Primitive sheet exhibits the lowest SD (narrowest distribution). It represents the best topology in terms of stress distribution but it exhibits the highest average stress (the worst among all). This means that the distribution of the Gyroid sheet is broader and the apparent σ_{max} is higher and closer to the apparent σ_{yield}. In this particular case, the apparent σ_{max} of the unit cells always remains lower than the $\sigma_{yield\_Bulk} = 830$ MPa because the stress range of the distributions is $0 - 350$ MPa.

On the contrary, the Gyroid sheet presents a lower weighted mean stress than the Primitive sheet. It must be pointed out that the volume fraction of the Gyroid sheet is also lower than the volume fraction of the Primitive sheet topology. Therefore, the selection of a TPMS-based lattice depends on the particular requirements to be addressed and there is not a unique solution. A solution is based on the application and a compromise between topology, volume fraction, stress state, etc. should be achieved.

Fig. 8 shows a ranking of the structures. As these structures are iso-elastic (same effective Young's modulus), the criterion for selecting the best structure depends on two aspects: (i) the bulk material density and (ii) the risks involved in the case of either cyclic or unusually high amplitude loading (proportional to the studied deformation field). The aim is to optimize the topologies by minimizing the effects of these two aspects. The interest of the R-factor is that it is a scalar and easily identifiable parameter, which allows, in a more general way, to compare a large number of structures between them. The Primitive sheet structure is the structure that clearly stands out in this ranking, since it minimises the R-factor (4.95) while being the structure whose density is closest to the density of the bone. It is worth noting that this structure has the highest average stress (0.263 in Table 2). On the other hand, the Gyroid sheet structure has the highest number of stress events above 150 MPa and represents the highest risk in case of abnormal loading.

5. Conclusions

In the present study, a full numerical global/local quantitative

approach is presented to replace a region of interest of a femoral bone (global model) with a TPMS-based unit cell (local model). The apparent elastic modulus distribution and the applied load on the 3D model correspond to a realistic stiffness distribution and loading case. The strain tensor has been extracted from the area of interest and applied to four unit cells towards a full investigation concerning various parameters. The objective is to define which topology is the most suitable for the replacement according to specific biomedical requirements.

It should be mentioned that the proposed methodology provides a general TPMS-based optimization framework. It aims at tailoring a TMPS structure for bone replacement. The developed methodology can be deployed to biomimic any type of bone using TPMS-based lattices, given the loading configuration. Furthermore, full stress and statistical analyses can be performed subsequently to the application of various boundary conditions as well. The study case of a partial bone replacement by a TPMS-based unit cell aims at describing all the steps of the design methodology and presenting the results that can lead to the selection of a suitable topology and the optimization of the structure.

In the present study, the primitive sheet was found to be the best structure that satisfies physiological and mechanical requirements. The following conclusions have been reached:

- Assigning real elastic properties to a bone and applying a real load to the FEA analysis results in a consistent prediction of the actual stress-strain state in the bone. The developed approach can be employed for further investigation of potential implant topologies to select the most suitable according to particular requirements.
- The actual strain of the real bone can be combined with periodic boundary conditions to provide a satisfactory approximation of the real physiological load on a given area of a bone.
- Four unit cell topologies with the appropriate apparent elastic moduli have been investigated to replace a part of a femoral bone as a multi-parameter problem. Due to the complexity of the problem, the non-uniqueness of the optimal solution has been shown. Depending on the requirements based on the patient's profile in terms of activities, age, etc., a different topology could be selected as the most appropriate compromise between the material solution and the loading configuration.
- The results of this study show that in the area of interest and for a physiological macroscopic load, the primitive sheet structure is the most appropriate. This replacement is customized according to the patient's profile, taking into account specific loading conditions. In a future work, the methodology developed in the present paper, will be deployed to build a database whose results would be dependent on the morphology of the patient, the type of mechanical loading and the area of the bone to be replaced.
- As the requirements to satisfy are defined by the position of the region of the bone to be replaced, different topologies and volume fractions can be selected for each region of the bone. The combination of the unit cell topologies may result in multi-morphology lattices [20] or macro-porosity gradient lattices that meet the local requirements in the most accurate way.

CRediT authorship contribution statement

Chrysoula Chatzigeorgiou: Writing – original draft, Validation, Methodology, Investigation, Formal analysis, Conceptualization. **Boris Piotrowski:** Writing – original draft, Resources, Methodology, Formal analysis, Conceptualization. **Fodil Meraghni:** Writing – review & editing, Validation, Supervision, Methodology, Investigation, Funding acquisition, Formal analysis, Conceptualization. **Yves Chemisky:** Writing – review & editing, Supervision, Methodology, Investigation, Formal analysis, Conceptualization.

Declaration of competing interest

The authors declare that they have no known competing financial interests or personal relationships that could have appeared to influence the work reported in this paper.

Acknowledgments

Data availability

Data will be made available on request.

References

[1] H.A. Almeida, P.J. da, Silva Bártolo, Mathematical modeling of 3D tissue engineering constructs, in: A. Ovsianikov, J. Yoo, V. Mironov (Eds.), 3D Printing and Biofabrication, Springer International Publishing, Cham, 2018, pp. 223–252, https://doi.org/10.1007/978-3-319-45444-3_5.

[2] M. Abdel-Hady Gepreel, M. Niinomi, Biocompatibility of Ti-alloys for long-term implantation, J. Mech. Behav. Biomed. Mater. 20 (2013) p407–p415, https://doi.org/10.1016/j.jmbbm.2012.11.014.

[3] J. Wolff, The Law of Bone Remodelling, Springer Berlin Heidelberg, Berlin, 1986, p. 2013, https://doi.org/10.1007/978-3-642-71031-5.

[4] C. Stewart, B. Akhavan, S.G. Wise, M.M.M. Bilek, A review of biomimetic surface functionalization for bone-integrating orthopedic implants: mechanisms, current approaches, and future directions, Prog Mater Sci 106 (2019) 100588, https://doi.org/10.1016/j.pmatsci.2019.100588.

[5] L. Yuan, S. Ding, C. Wen, Additive manufacturing technology for porous metal implant applications and triple minimal surface structures: a review, Bioact. Mater. 4 (2019) 56–70, https://doi.org/10.1016/j.bioactmat.2018.12.003.

[6] W. Elmay, E. Patoor, B. Bolle, T. Gloriant, F. Prima, A. Eberhardt, P. Laheurte, Optimisation of mechanical properties of Ti–Nb binary alloys for biomedical applications, Comput. Methods Biomech. Biomed. Eng. 14 (2011) 119–120, https://doi.org/10.1080/10255842.2011.593760.

[7] P. Laheurte, F. Prima, A. Eberhardt, T. Gloriant, M. Wary, E. Patoor, Mechanical properties of low modulus ββ titanium alloys designed from the electronic approach, J. Mech. Behav. Biomed. Mater. 3 (2010) 565–573, https://doi.org/10.1016/j.jmbbm.2010.07.001.

[8] E. Alabort, D. Barba, R.C. Reed, Design of metallic bone by additive manufacturing, Scr. Mater. 164 (2019) 110–114, https://doi.org/10.1016/j.scriptamat.2019.01.022.

[9] B. Piotrowski, A.A. Baptista, E. Patoor, P. Bravetti, A. Eberhardt, P. Laheurte, Interaction of bone–dental implant with new ultra low modulus alloy using a numerical approach, Mater. Sci. Eng. C 38 (2014) 151–160, https://doi.org/10.1016/j.msec.2014.01.048.

[10] M.F. Ashby, The properties of foams and lattices, Phil. Trans. R. Soc. A. 364 (1838) (2006) 15–30, https://doi.org/10.1098/rsta.2005.1678.

[11] X.P. Tan, Y.J. Tan, C.S.L. Chow, S.B. Tor, W.Y. Yeong, Metallic powder-bed based 3D printing of cellular scaffolds for orthopaedic implants: a state-of-the-art review on manufacturing, topological design, mechanical properties and biocompatibility, Mater. Sci. Eng. C 76 (2017) 1328–1343, https://doi.org/10.1016/j.msec.2017.02.094.

[12] A.H. Schoen, Infinite Periodic Minimal Surfaces Without Self-Intersections, NASA, 1970. Technical Note No. TN D-5541.

[13] P.J.F. Gandy, J. Klinowski, Exact computation of the triply periodic Schwarz P minimal surface, Chem. Phys. Lett. 322 (6) (2000) 579–586, https://doi.org/10.1016/S0009-2614(00)00453-X.

[14] P.J.F. Gandy, J. Klinowski, Exact computation of the triply periodic G (ˈGyroid') minimal surface, Chem. Phys. Lett. 321 (5–6) (2000) 363–371, https://doi.org/10.1016/S0009-2614(00)00373-0.

[15] M. Pelanconi, A. Ortona, Nature-Inspired, ultra-lightweight structures with gyroid cores produced by additive manufacturing and reinforced by unidirectional carbon fiber ribs, Materials (Basel) 12 (24) (2019) 4134, https://doi.org/10.3390/ma12244134.

[16] S.A. Tyagi, M. Manjaiah, Additive manufacturing of titanium-based lattice structures for medical applications – a review, Bioprinting 30 (2023) e00267, https://doi.org/10.1016/j.bprint.2023.e00267.

[17] C. Chatzigeorgiou, B. Piotrowski, Y. Chemisky, P. Laheurte, F. Meraghni, Numerical investigation of the effective mechanical properties and local stress distributions of TPMS-based and strut-based lattices for biomedical applications, J. Mech. Behav. Biomed. Mater. 126 (2022) 105025, https://doi.org/10.1016/j.jmbbm.2021.105025.

[18] S. Kanwar, S. Vijayavenkataraman, Design of 3D printed scaffolds for bone tissue engineering: a review, Bioprinting 24 (2021) e00167, https://doi.org/10.1016/j.bprint.2021.e00167.

[19] O. Al-Ketan, D.W. Lee, R. Rowshan, R.K. Abu Al-Rub, Functionally graded and multi-morphology sheet TPMS lattices: design, manufacturing, and mechanical properties, J. Mech. Behav. Biomed. Mater. 102 (2020) 103520, https://doi.org/10.1016/j.jmbbm.2019.103520.

[20] H. Xi, Z. Zhou, H. Zhang, S. Huang, H. Xiao, Multi-morphology TPMS structures with multi-stage yield stress platform and multi-level energy absorption: design, manufacturing, and mechanical properties, Eng. Struct. 294 (2023) 116733, https://doi.org/10.1016/j.engstruct.2023.116733.

[21] R. Havaldar, S. Pilli, B. Putti, Insights into the effects of tensile and compressive loadings on human femur bone, Adv. Biomed. Res. 3 (1) (2014) 101, https://doi.org/10.4103/2277-9175.129375.

[22] M. Niinomi, M. Nakai, Titanium-based biomaterials for preventing stress shielding between implant devices and bone, Int. J. Biomater. 2011 (2011) 1–10, https://doi.org/10.1155/2011/836587.

[23] W. Solórzano, C. Ojeda, A. Diaz Lantada, Biomechanical study of proximal femur for designing stems for total hip replacement, Appl. Sci. 10 (12) (2020) 4208, https://doi.org/10.3390/app10124208.

[24] Y. Jun, K. Choi, Design of patient-specific hip implants based on the 3D geometry of the human femur, Adv. Eng. Softw. 41 (4) (2010) 537–547, https://doi.org/10.1016/j.advengsoft.2009.10.016.

[25] J.M. Haglin, A.E.M. Eltorai, J.A. Gil, S.E. Marcaccio, J. Botero-Hincapie, A.H. Daniels, Patient-Specific orthopaedic implants: orthopaedic Implants, Orthop. Surg. 8 (4) (2016) 417–424, https://doi.org/10.1111/os.12282.

[26] M.I. Mohammed, A.P. Fitzpatrick, I. Gibson, Customised design of a patient specific 3D printed whole mandible implant, KEG 2 (2) (2017) 104, https://doi.org/10.18502/keg.v2i2.602.

[27] M. Rezapourian, I. Jasiuk, M. Saarna, I. Hussainova, Selective laser melted Ti6Al4V split-P TPMS lattices for bone tissue engineering, Int. J. Mech. Sci. 251 (2023) 108353, https://doi.org/10.1016/j.ijmecsci.2023.108353.

[28] M. Vafaeefar, K.M. Moerman, M. Kavousi, T.J. Vaughan, A morphological, topological and mechanical investigation of gyroid, spinodoid and dual-lattice algorithms as structural models of trabecular bone, J. Mech. Behav. Biomed. Mater. 138 (2023) 105584, https://doi.org/10.1016/j.jmbbm.2022.105584.

[29] N. Elenskaya, M. Tashkinov, I. Vindokurov, Y. Pirogova, V.V. Silberschmidt, Understanding of trabecular-cortical transition zone: numerical and experimental assessment of multi-morphology scaffolds, J. Mech. Behav. Biomed. Mater. 147 (2023) 106146, https://doi.org/10.1016/j.jmbbm.2023.106146.

[30] N. Yang, H. Wei, Z. Mao, Tuning surface curvatures and young's moduli of TPMS-based lattices independent of volume fraction, Mater. Des. 216 (2022) 110542.

[31] E. Maevskaia, J. Guerrero, C. Ghayor, I. Bhattacharya, F.E. Weber, Triply periodic minimal surface-based scaffolds for bone tissue engineering: a mechanical, in vitro and in vivo study, Tissue Eng. Part A 19-20 (2023) 507–517, https://doi.org/10.1089/ten.TEA.2023.0033.

[32] K.C. Wong, 3D-printed patient-specific applications in orthopedics, ORR 8 (2016) 57–66, https://doi.org/10.2147/ORR.S99614.

[33] J. Jin, S. Wu, L. Yang, C. Zhang, Y. Li, C. Cai, C. Yan, Y. Shi, Ni–Ti multicell interlacing Gyroid lattice structures with ultra-high hyperelastic response fabricated by laser powder bed fusion, Int. J. Mach. Tools Manuf. 195 (Part B) (2024) 104099, https://doi.org/10.1016/j.ijmachtools.2023.104099.

[34] K. Rezapourian, R. Kumar, I. Hussainova, Effect of unit cell rotation on mechanical performance of selective laser melted Gyroid structures for bone tissue engineering, Prog. Eng. Sci. 1 (2024) 100011, https://doi.org/10.1016/j.pes.2024.100011.

[35] T.D. DenOtter, J. Schubert, Hounsfield Unit. StatPearls, StatPearls Publishing, Treasure Island (FL), 2021. Accessed: Nov. 23, 2021. [Online]. Available: http://www.ncbi.nlm.nih.gov/books/NBK547721/.

[36] N. Okkalidis, C. Chatzigeorgiou, D. Okkalides, Assessment of 11 available materials with custom three-dimensional-printing patterns for the simulation of muscle, fat, and lung housnfield units in patient-specific phantoms, J. Eng. Sci. Med. Diagn. Ther. 1 (1) (2018) 011003, https://doi.org/10.1115/1.4038228.

[37] M. Helou, S. Kara, Design, analysis and manufacturing of lattice structures: an overview, Int. J. Comput. Integr. Manuf. 31 (3) (2018) 243–261, https://doi.org/10.1080/0951192X.2017.1407456.

[38] S.N. Khan, R.M. Warkhedkar, A.K. Shyam, Analysis of hounsfield unit of human bones for strength evaluation, Procedia Mater. Sci. 6 (2014) 512–519, https://doi.org/10.1016/j.mspro.2014.07.065.

[39] J.Y. Rho, M.C. Hobatho, R.B. Ashman, Relations of mechanical properties to density and CT numbers in human bone, Med. Eng. Phys. 17 (5) (1995) 347–355, https://doi.org/10.1016/1350-4533(95)97314-F.

[40] V.N. Chougule, A.V. Mulay, B.B. Ahuja, Clinical Case Study: Spine Modeling for Minimum Invasive Spine Surgeries (MISS) using Rapid Prototyping, in: presented at the Proceedings of 10th International Conference on Precision, Meso, Micro and Nano Engineering (COPEN 10) December 07-09, 2017, Indian Institute of Technology Madras, 2018. Chennai-600 036 INDIA.

[41] M.J. Ciarelli, S.A. Goldstein, J.L. Kuhn, D.D. Cody, M.B. Brown, Evaluation of orthogonal mechanical properties and density of human trabecular bone from the major metaphyseal regions with materials testing and computed tomography, J. Orthop. Res. 9 (5) (1991) 674–682, https://doi.org/10.1002/jor.1100090507.

[42] P. Bazyar, E. Sheidaee, Design and simulating lattice structures in the FE analysis of the femur bone, Bioprinting 37 (2024) e00326, https://doi.org/10.1016/j.bprint.2023.e00326.

[43] 'https://orthoload.com/'.

[44] D.T. Reilly, A.H. Burstein, The elastic and ultimate properties of compact bone tissue, J. Biomech. 8 (6) (1975) 393–405, https://doi.org/10.1016/0021-9290(75)90075-5.

[45] E.F. Morgan, G.U. Unnikrisnan, A.I. Hussein, Bone mechanical properties in healthy and diseased states, Annu. Rev. Biomed. Eng. 20 (1) (2018) 119–143, https://doi.org/10.1146/annurev-bioeng-062117-121139.

[46] M.O. Heller, et al., Musculo-skeletal loading conditions at the hip during walking and stair climbing, J. Biomech. 34 (7) (2001) 883–893, https://doi.org/10.1016/S0021-9290(01)00039-2.

[47] G. Bergmann, A. Bender, J. Dymke, G. Duda, P. Damm, Standardized loads acting in hip implants, PLoS ONE 11 (5) (2016) e0155612, https://doi.org/10.1371/journal.pone.0155612.

[48] M. Fischer, 'Élaboration in situ d'alliages de titane et de structures architecturées par fabrication additive : application aux dispositifs médicaux implantables'. 2017. [in French].

[49] 'https://www.nlm.nih.gov/'.

[50] I. Maskery, A.O. Aremu, L. Parry, R.D. Wildman, C.J. Tuck, I.A. Ashcroft, Effective design and simulation of surface-based lattice structures featuring volume fraction and cell type grading, Mater. Des. 155 (2018) 220–232, https://doi.org/10.1016/j.matdes.2018.05.058.

[51] F. Praud, G. Chatzigeorgiou, F. Meraghni, Fully integrated multi-scale modelling of damage and time-dependency in thermoplastic-based woven composites, Int. J. Damage Mech. (2020), https://doi.org/10.1177/1056789520944986, 105678952094498.

[52] P.M. Suquet, Elements of homogenization for inelastic solid mechanics, in: Lecture Notes in Physics, 272, Springer, Berlin, 1987, pp. 193–278.

[53] 'https://www.azom.com/article.aspx?ArticleID=9299'.